

Full length article

Quasi-free-standing epitaxial graphene on 4H-SiC(0001) as a two-dimensional reference standard for Kelvin Probe Force Microscopy

Tymoteusz Ciuk^{a,*}, Beata Pyrzanowska^a, Jakub Jagiełło^a, Artur Dobrowolski^a, Dariusz Czołak^a, Maciej J. Szary^b

^a Łukasiewicz Research Network - Institute of Microelectronics and Photonics, al. Lotników 32/46, 02-668 Warsaw, Poland

^b Institute of Physics, Poznan University of Technology, Piotrowo 3, 61-138 Poznan, Poland

ARTICLE INFO

Keywords:

Graphene
Epitaxy
CVD
SiC
Kelvin probe
Surface potential
Work function
Reference standard

ABSTRACT

Kelvin Probe Force Microscopy is a method to assess the contact potential difference between a sample and the probe tip. It remains a relative tool unless a reference standard with a known work function is applied, typically bulk gold or cleaved highly oriented pyrolytic graphite. In this report, we suggest a verifiable, two-dimensional standard in the form of a photolithographically patterned, wire-bonded structure manufactured in the technology of transfer-free p-type hydrogen-intercalated quasi-free-standing epitaxial Chemical Vapor Deposition graphene on semi-insulating high-purity nominally on-axis 4H-SiC(0001). The particular structure has its hole density $p_S = 1.61 \times 10^{13} \text{ cm}^{-2}$ measured through a classical Hall effect, its number of the graphene layers $N = 1.74$ extracted from the distribution of the ellipsometric angle Ψ , measured at the angle of incidence $\text{AOI} = 50^\circ$ and the wavelength $\lambda = 490 \text{ nm}$, and its work function $\phi_{GR} = 4.79 \text{ eV}$ postulated by a Density Functional Theory model for the specific p_S and N . Following the algorithm, the contact potential difference between the structure and a silicon tip, verified at $\Delta V_{GR-Si} = 0.64 \text{ V}$, ought to be associated with $\phi_{GR} = 4.79 \text{ eV}$ and applied as a precise reference value to calculate the work function of an arbitrary material.

1. Introduction

The Kelvin Probe Force Microscopy (KPFM), or surface potential microscopy, is a powerful tool to assess the contact potential difference (ΔV_{m-Si}) between two materials characterized by different work functions, typically the material under study (ϕ_m) and the silicon tip of a lever probe (ϕ_{Si}). It is a relative method unless a reference material is available with a known work function (ϕ_{REF}), calibrated with other than the KPFM method, e.g., ultraviolet photoelectron spectroscopy [1] or angle-resolved photoelectron spectroscopy [2]. Then, the contact potential difference between the reference material and the tip, or ΔV_{REF-Si} , can be calculated into the work function of the material under study, or $\phi_m = \phi_{REF} + e(V_{m-Si} - V_{REF-Si})$, where e is the unit charge.

Several bulk materials serve the purpose of reference standards, including gold and highly oriented pyrolytic graphite (HOPG) [3–5]. Gold is in value as a referential material due to its high chemical inertness; however, the contamination resulting from storage conditions and the sample cleaning methods impacts its work function (ϕ_{Au}). Its values can range from 4.4 eV to 5.4 eV [6–8], and even with precautions in storing conditions, the ϕ_{Au} would yield a 4.75 eV to 5.25 eV dispersion [9]. Also, the structure of gold (amorphous vs.

polycrystalline with randomly oriented crystallites) influences the ϕ_{Au} with reported values Au(111): 5.3 eV, Au(311): 5.16 eV, Au(110): 5.12 eV, and Au(210): 4.96 eV [10].

HOPG, due to its atomic flatness, lack of surface reconstruction, and the absence of dangling bonds, is considered more stable than gold and, therefore, preferable as the reference standard [11,12]. However, HOPG also proved to be sensitive to ambient conditions [12], with its ϕ_{HOPG} ranging from 4.48 eV to 5.0 eV [13–16]. Yet, unlike gold, HOPG can be repeatedly refreshed through direct exfoliation (cleaving) of the topmost carbon layers.

In this work, we verify a two-dimensional carbon material as a reference standard for the KPFM method, possibly a complement to bulk gold and cleaved HOPG. The material is transfer-free p-type hydrogen-intercalated quasi-free-standing (QFS) epitaxial Chemical Vapor Deposition (CVD) graphene on semi-insulating high-purity nominally on-axis 4H-SiC(0001).

This form of carbon material offers a range of properties that enable one to assign it a precise, theory-based work function. These include the two-dimensional character, atomic-flat surface within the (0001) terraces [17,18], elemental purity, lack of substitutional dopants or

* Corresponding author.

E-mail address: tymoteusz.ciuk@imif.lukasiewicz.gov.pl (T. Ciuk).

post-transfer organic residue [19], and uniformity of charge carrier type and sheet density determined by the substrate-related vector of spontaneous polarization [20,21].

Critically, though, and contrary to gold and HOPG, the structural and transport properties of QFS-graphene/4H-SiC(0001) are directly and frequently measurable through spectroscopic ellipsometry [22] and the classical Hall effect [17,18]. Also, a lithographically patterned, wire-bonded QFS-graphene/4H-SiC(0001) structure enables efficient connection to the apparatus signal ground and, thus, charge sinking.

We introduce a practical algorithm in the course of which a QFS-graphene/4H-SiC(0001) structure has its statistical distribution of the number of the QFS graphene layers N [19,23] (typically a fractional number between 1.0 and 2.0) extracted from an ellipsometric analysis [22], its hole density p_S outright measured in a Hall effect setup, and its work function ϕ_{GR} numerically calculated via a Density Functional Theory (DFT) model for the previously determined p_S and N . With this knowledge, the apex of the measured contact potential difference distribution between the QFS graphene and the silicon tip, or ΔV_{GR-Si} , can be used as a precise reference standard to calculate the work function of any other material under study, or $\phi_m = \phi_{GR} + e(V_{m-Si} - V_{GR-Si})$.

Following our experience with the amorphous- Al_2O_3 /QFS-graphene/4H-SiC(0001) Hall effect sensor [24], the reproducibility of the QFS-graphene/4H-SiC(0001) structure transport properties within a single processing cycle is estimated at $\sim 10\%$, measured as a percentile ratio of standard deviation over mean value ($\sigma/mean \times 100\%$). This variation is considered low for graphene technology and possible only because direct epitaxial growth is superior to a polymer-assisted transfer [19]. The vestigial dispersion is a remnant of the fingerprint-like topography of epitaxial graphene, marked with a combination of micrometer-scale terraces and nanometer-high steps [17,18,25]. These, in turn, originate from the fact that although nominally on-axis, the as-purchased SiC wafer is never ideally oriented along the [0001] vector.

Nevertheless, the SiC wafer miscut, the CVD growth reproducibility, or the processing reproducibility are not critical as the protocol assumes each QFS-graphene/4H-SiC(0001) structure has its unique p_S and N individually verified and projected onto the DFT-calculated ϕ_{GR} chart, before serving as the KPFM reference standard. Also, the element is frequently regenerable through thermally-assisted desorption in vacuum conditions (up to 500 °C [24]) and may have its electrical properties updated. For these reasons, we dedicate our algorithm to research and development centers and semiconductor manufacturers operating under demanding time frames and pressure for optimization.

2. Experimental details

2.1. Graphene CVD epitaxy and the mesa structure technology

The transfer-free p-type hydrogen-intercalated quasi-free-standing graphene [22] was grown epitaxially on a semi-insulating (SI) high-purity (HP) nominally on-axis 500- μm -thick 20-mm \times 20-mm 4H-SiC(0001) sample cut from a 4-in wafer purchased at Wolfspeed, Inc. The growth was conducted in an Aixtron VP508 reactor at 1600 °C, using Chemical Vapor Deposition (CVD) in argon flow [26] and thermally decomposed propane as the carbon-sourcing gas. The growth was preceded by *in-situ* etching of the SiC(0001) surface in a pure hydrogen atmosphere at 1600 °C and chamber pressure of 100 mbar, and followed by *in-situ* hydrogen intercalation [27] at 1000 °C under 900-mbar argon atmosphere.

Then, through a series of optical lithography-based steps involving metal deposition and oxygen plasma etching, the surface of the sample was processed into 96 1.4-mm \times 1.4-mm four-terminal *van der Pauw* elements [23], each featuring an oxygen-plasma-etched, cross-shaped [28] 100- μm \times 300- μm (50 000 μm^2) QFS graphene mesa against plasma-exposed 4H-SiC(0001) and electron-beam-deposited Ti/Au (10

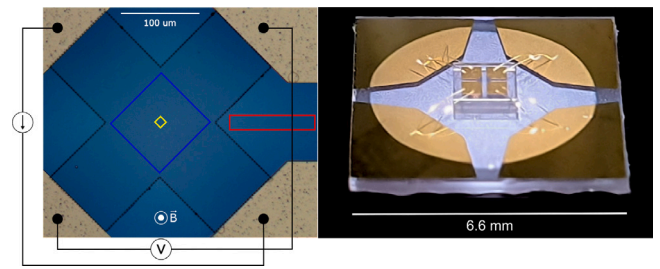


Fig. 1. (a) Nomarski interference contrast optical image of the four-terminal element featuring a cross-shaped 100- μm \times 300- μm hydrogen-intercalated QFS epitaxial CVD graphene mesa against semi-insulating high-purity on-axis 4H-SiC(0001). For clarity, a black dashed line highlights the graphene mesa. Marked in blue is the 90- μm \times 90- μm region intended for the extraction of the ellipsometric Ψ angle distribution within the QFS graphene mesa, and red is the 110- μm \times 20- μm region for the extraction of Ψ within the exposed 4H-SiC(0001), and yellow is the 10- μm \times 10- μm region for the KPFM analysis. The wiring schematically illustrates the direct current feed and the voltage readout during the Hall effect measurement in a perpendicular magnetic field. (b) Photograph of the mounted and wire-bonded QFS-graphene/4H-SiC(0001) structure.

nm/110 nm) current feed and voltage readout contacts. In this experiment, one of the *van der Pauw* elements was mounted onto and gold-wire-bonded to a custom-made 6.6-mm \times 6.6-mm 364- μm -thick sapphire holder equipped with four Ti/Au (10 nm/190 nm) corner contacts enabling electrical characterization. Fig. 1 depicts the optical image. Markings enrich the image to trace the location of the subsequent ellipsometric (blue and red) and Kelvin Probe Force Microscopy (yellow) analyses.

2.2. Hall effect characterization of the QFS graphene

The room-temperature electrical characterization of the four-terminal element was conducted under $I = 1\text{-mA}$ direct current bias in an 0.556-T Ecopia AHT55T5 automated Hall effect measurement system operating *van der Pauw* formulae and a single-carrier transport model. The measurement revealed the graphene-related hole density p_S [cm^{-2}], hole mobility μ_p [cm^2/Vs], and sheet resistance R_S [Ω/sq], all averaged over the 50 000- μm^2 area of the cross-shaped QFS mesa.

2.3. Ellipsometric model and analysis of the number of the QFS graphene layers

To determine the statistical number of the QFS graphene layers N , we employed an ellipsometric protocol, initially introduced in Ref. [22] for hydrogen-intercalated QFS epitaxial CVD graphene on semi-insulating vanadium-compensated nominally on-axis 6H-SiC(0001).

The Accurion EP4SE spectral imaging ellipsometer equipped with a Nanochromat NC2 UV-VIS-NIR microscope objective and operating in the nulling regime was used to collect the ellipsometric angles, Ψ and Δ , defined through the ratio ρ of the Fresnel reflection coefficients:

$$\rho = \frac{r_p}{r_s} = \tan\Psi e^{i\Delta}$$

where r_p is the complex reflection coefficient for the electric field vector polarized parallel to the plane of incidence and r_s is the complex reflection coefficient for the electric field vector polarized perpendicular. The protocol assumed optimum measurement conditions at the angle of incidence AOI = 50° and the wavelength $\lambda = 490$ nm for both ellipsometric angles.

Two areas were chosen for the extraction of the Ψ and Δ distributions, one of them entirely within the QFS graphene mesa (90- μm \times 90- μm blue square in Fig. 1) and one referential within exposed 4H-SiC(0001) (110- μm \times 20- μm red rectangle in Fig. 1).

To extract the number of the QFS graphene layers N , we applied the protocol from Ref. [22], postulating the following form of the Fresnel reflection coefficients r_p and r_s :

$$r_p = \frac{n_1 \cos \theta_i - n_2 \cos \theta_t - 2N \pi \alpha \cos \theta_i \cos \theta_t}{n_1 \cos \theta_i + n_2 \cos \theta_t + 2N \pi \alpha \cos \theta_i \cos \theta_t} \quad (1)$$

$$r_s = \frac{n_1 \cos \theta_i - n_2 \cos \theta_t + 2N \pi \alpha}{n_1 \cos \theta_i + n_2 \cos \theta_t + 2N \pi \alpha} \quad (2)$$

where n_1 and n_2 represent refractive indices at the phase boundary, and θ_i and $\theta_t = \arcsin(\frac{n_1 \sin \theta_i}{n_2})$, are the angles of incidence and transmission, respectively. In our experiment, the n_1 describes the air; therefore, set at $n_1 = 1$. The n_2 describes the 4H-SiC(0001) substrate and is a real number.

2.4. Density functional theory model and calculation of the QFS graphene work function

Material modeling of monolayer, bilayer, and trilayer QFS graphene was conducted using a two-dimensional periodic slab in a 3×3 supercell, with approximately 25 Å inter-slab vacuum along [001] in each case to avoid periodic image problems and to produce regions with well-defined vacuum potential. Bi- and trilayers employed AB and ABA stacking, respectively. All computations for this study utilized density functional theory with plane waves, pseudopotentials, and the projector-augmented wave (PAW) method, as implemented in the QUANTUM ESPRESSO suite [29–31].

The pseudopotentials included scalar-relativistic and nonlinear core corrections. The plane-wave cutoff energies for the wave function and electron density were set at 60 and 600 Ry, respectively. Brillouin zone integration of the supercell used an $8 \times 8 \times 1$ Monkhorst–Pack grid [32]. Tests were conducted to assess optimal cutoff energies, and k-point grids with higher values showed minimal impact on the modeled properties. During structure optimization, all the atom positions were adjusted until the force reached a convergence criterion of less than 10^{-4} Ry/au and the total energy reached a convergence criterion of less than 10^{-5} Ry. For approximating the electron exchange–correlation energy, the Heyd–Scuseria–Ernzerhof (HSE) hybrid functional was employed [33], as it has been shown in previous studies to enable accurate modeling of the work function in graphene [34]. Hole density in the model systems was controlled by modulating their total charge. Consequently, all computations were performed with unrestricted spin, as some model cases had an odd number of electrons.

The theoretical work function is calculated by taking the difference of vacuum energy ($E_{\text{vac}} = eV_{\text{vac}}$) relative to Fermi energy (E_F) [34]

$$\phi_{GR} = eV_{\text{vac}} - E_F. \quad (3)$$

Fermi energy is obtained directly from the self-consistent-field calculations. The vacuum potential is obtained by calculating the planar average of the electrostatic potential across the supercell and taking its value sufficiently far from the surface along the [001] direction.

2.5. Kelvin probe force microscopy analysis of the QFS graphene contact potential difference

The contact potential difference (CPD) was collected with the Bruker Dimension Icon equipment. The measurements were performed at ambient conditions (exposure to air, room temperature) using PFQNE-AL probes (silicon tip on a silicon nitride cantilever) provided by Bruker (resonant frequency = 300 kHz, $k = 0.8 \text{ Nm}^{-1}$). The CPD images and corresponding data histograms were collected using the amplitude modulation mode. The scan area was $10 \mu\text{m} \times 10 \mu\text{m}$ within the center of the QFS graphene mesa (yellow region in Fig. 1) and 512×512 points with a 0.326-Hz scan rate. During the temporal stability tests, the scan area was reduced to $5 \mu\text{m} \times 5 \mu\text{m}$ and 256×256 points with a 0.498-Hz scan rate to possibly equalize the temporal conditions.

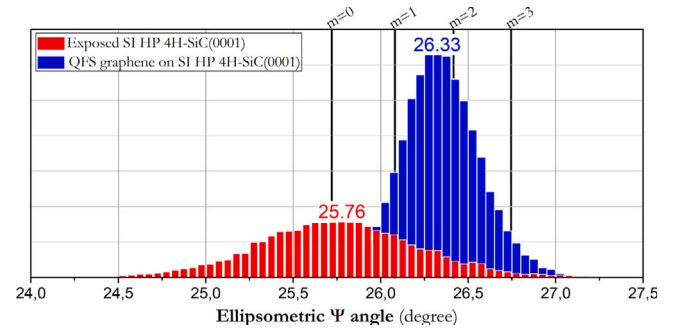


Fig. 2. (a) Distribution of the ellipsometric angle Ψ within the QFS graphene mesa (blue) and the exposed 4H-SiC(0001) substrate (red), measured at AOI = 50° and $\lambda = 490 \text{ nm}$, within the subareas marked in Fig. 1. The vertical solid lines indicate Ψ angle expected for a single, two, and three QFS graphene layers based on our model.

3. Results and discussion

3.1. Hall-effect-derived hole density in the QFS graphene

The four-terminal element was biased with $I = 1\text{-mA}$ direct current and tested at room temperature in an 0.556-T Ecopia AHT55T5 automated Hall effect measurement system. The measurement confirmed p-type doping induced by the substrate-related [20] positive polarization quantified by vector $P^{AH} = -2.0 \times 10^{-2} \text{ C/m}^2$ [21] through $p_S^{AH} = -P_0^{AH}/e = 1.2 \times 10^{13} \text{ cm}^{-2}$, where e is the unit charge. The hole density was estimated at p_S at $1.61 \times 10^{13} \text{ cm}^{-2}$, along with hole mobility $\mu_p = 1681 \text{ cm}^2/\text{Vs}$ and sheet resistance $R_S = 230 \Omega/\text{sq}$.

The p_S has a statistical meaning as it is average over the $50000\text{-}\mu\text{m}^2$ area of the cross-shaped mesa. Also, it is outside the conventional commercial range of $1.2\text{--}1.3 \times 10^{13} \text{ cm}^{-2}$ (GET® [35]) but in agreement with the historical scientific spread beyond the theoretical value of $p_S^{AH} = 1.2 \times 10^{13} \text{ cm}^{-2}$ [17,18]. It will be illustrated in the subsequent DFT section that the variations of hole density above the theoretical $p_S^{AH} = 1.2 \times 10^{13} \text{ cm}^{-2}$ ($1.2\text{--}2.0 \times 10^{13} \text{ cm}^{-2}$) have only a marginal effect on the QFS graphene work function.

3.2. Ellipsometry-derived statistical number of the QFS graphene layers

In the domain of Ψ , the data associated with the QFS graphene mesa are located between $\Psi = 25.5^\circ$ and $\Psi = 27.5^\circ$. The distribution peak (apex of a Gaussian fit) is at $\Psi = 26.33^\circ$ with a standard deviation $\sigma = 0.21^\circ$. Data related to the plasma-etched, exposed 4H-SiC(0001) span the range between $\Psi = 24.0^\circ$ and $\Psi = 27.5^\circ$, with the peak at $\Psi = 25.76^\circ$. Therefore, the presence of QFS graphene appears to have up-shifted Ψ by 0.57° (Fig. 2). The up-shift is higher than previously reported for close-to-perfect-monolayer QFS graphene, 0.33° in Ref. [22], already suggesting more than a single QFS layer.

According to our model, $\Psi = 25.76^\circ$ measured at AOI = 50° and $\lambda = 490 \text{ nm}$ outside of the graphene mesa suggests that the real-number refractive index of the 4H-SiC(0001) substrate is $n_2 = 2.72$. Based on this, $\Psi = 25.76^\circ$ within the QFS graphene translates into statistically $N = 1.74$ layers. The $N = 1.74$ lies within the historically witnessed range for QFS graphene on SiC(0001), which spans the values from $N \sim 1.0$ and $N \sim 2.0$ and is close to the expected statistical value for this technology of $N \sim 1.5$.

The reason that the layer composition is a fractional value is the developed surface of the substrate. Although nominally on-axis, the as-purchased SiC(0001) wafer is never ideally oriented along the [0001] vector. As a result, it is slightly off-axis (up to 0.2°), and once in-situ-etched, its surface reveals micrometer-scale (0001) terraces separated by few-nanometer-high steps [17,18,25]. These offer uneven growth conditions and favor additional graphene inclusions at SiC vicinal surfaces, making each QFS-graphene-on-SiC(0001) sample topographically unrepeatable, similar to a human fingerprint. Hence, the direct verification of N within the specific mesa structure.

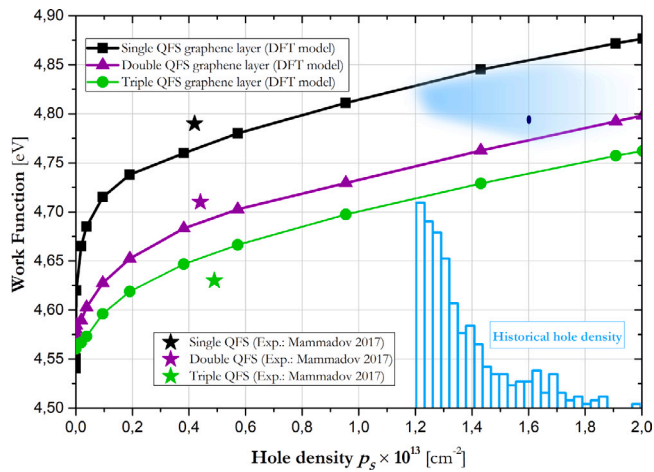


Fig. 3. Density-Functional-Theory-calculated-work function of a single, double, and triple QFS graphene layer as a function of hole density. The light blue cloud (rightward fading polygon) limits the expected N , p_S , and Φ_{GR} for the QFS-graphene/4H-SiC(0001) technology based on the own experience. The dark blue spot is the position of the QFS graphene under study based on the Hall effect measurement and the spectroscopic ellipsometry analysis. The inset histogram illustrates the historical distribution of hole density above the theoretical $p_S^{AH} = 1.2 \times 10^{13} \text{ cm}^{-2}$ based on Ref. [17] and Ref. [18]. The star-shaped points are single experimental data assessed with angle-resolved photoelectron spectroscopy for a comparable system and reproduced from Ref. [2].

3.3. DFT-calculated work function of the QFS graphene

According to the DFT model, the work function of QFS graphene (Φ_{GR}) is monotonically increasing with hole density. Away from the Dirac point, its values are lower in a double QFS layer than in a single QFS layer and even lower as one adds the third QFS layer (Fig. 3). This model considers only whole numbers of layers N . Still, we assume that fractional N will translate into intermediary values of Φ_{GR} . Also, given the tilt of the curves, a broad modification of N within the 1.0–2.0 range appears to affect Φ_{GR} by only 0.08 eV, which proves in favor of the method. For the statistically 1.74-layer QFS graphene characterized by hole density $p_S = 1.61 \times 10^{13} \text{ cm}^{-2}$, the Φ_{GR} reaches 4.79 eV (dark blue spot in Fig. 3).

The light blue cloud in Fig. 3 illustrates the conventional range of N and p_S for the QFS-graphene/4H-SiC(0001) technology. It is drawn based on the historically observed p_S [17,18], only down-trimmed to the theoretical $p_S^{AH} = 1.2 \times 10^{13} \text{ cm}^{-2}$. The statistical number of the QFS graphene layers N is unavailable for these points, yet it typically falls within the range between $N = 1.0$ and $N = 2.0$.

Also, this technology displays pronounced hole mobility vs. hole density inversion [17,18]. By experience, a high-mobility sample likely has its N closer to 1.0 and its p_S closer to the p_S^{AH} . Contrary to that, a low-mobility sample has its N closer to 2.0 and its p_S above the p_S^{AH} . So far, we have observed the lowest $N = 1.05$ in QFS graphene grown on semi-insulating vanadium-compensated 6H-SiC(0001) [22], with $\mu = 5019 \text{ cm}^2/\text{Vs}$ and with $p_S = 7.69 \times 10^{12} \text{ cm}^{-2}$, only slightly above $p_S^{AH} = 7.5 \times 10^{12} \text{ cm}^{-2}$ [21].

Since p_S close to the p_S^{AH} is unexpected in a double QFS layer and vice-versa, p_S away from p_S^{AH} has not been associated with a single QFS layer, the light blue cloud is arbitrarily a rightward fading polygon. Yet, to the advantage of the idea, within the spectrum of the expected N and p_S for the QFS-graphene/4H-SiC(0001) technology ($N = 1.0$ to 2.0, $p_S = 1.2$ to $2.0 \times 10^{13} \text{ cm}^{-2}$), the theorized work function falls within a relatively narrow $< 0.1\text{-eV}$ range between $\Phi_{GR} = 4.77 \text{ eV}$ and $\Phi_{GR} = 4.85 \text{ eV}$.

The DFT model is additionally confronted with experimental data for a single, double, and triple QFS graphene layer grown through sublimation in an argon atmosphere on conducting n-type 6H-SiC(0001)

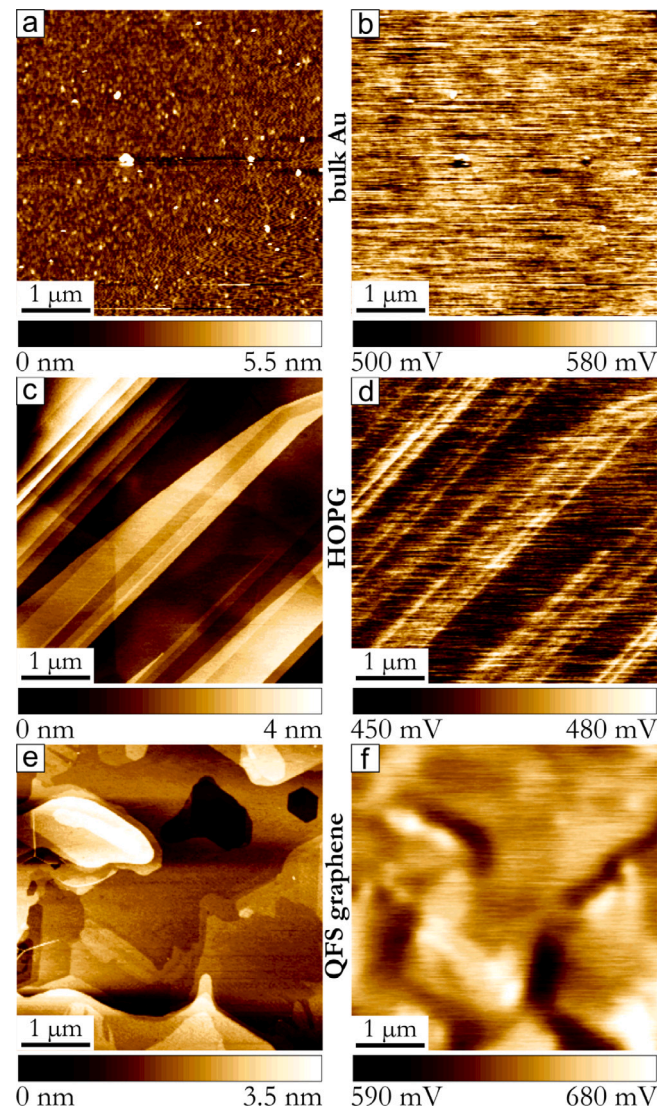


Fig. 4. $5\text{-}\mu\text{m} \times 5\text{-}\mu\text{m}$ maps of topography ((a), (c), (e)) and contact potential difference against the silicon tip ((b), (d), (f)) of commercial bulk Au standard, highly oriented pyrolytic graphite (HOPG), and the QFS graphene, respectively.

(bulk electron concentration $n = 5 \times 10^{17} \text{ cm}^{-3}$). The data (hole density and work function) are reproduced from Ref. [2] and were assessed with angle-resolved photoelectron spectroscopy. Even though the two QFS systems differ in the substrate, the experiment (star-shaped points in Fig. 3) corresponds to the theoretical model.

3.4. KPFM-derived relative contact potential of the QFS graphene

Collected in possibly close temporal conditions, the topographical and CPD maps of a commercial bulk gold standard, highly oriented pyrolytic graphite, and QFS graphene reveal structural and potential differences between the three reference materials (Fig. 4).

The contact potential difference between the QFS graphene and the silicon tip of the silicon nitride cantilever (ΔV_{GR-Si}) spans the range between $\Delta V_{GR-Si} = 0.56 \text{ V}$ and $\Delta V_{GR-Si} = 0.71 \text{ V}$, with the distribution peak (apex of a Gaussian fit) at $\Delta V_{GR-Si} = 0.64 \text{ V}$ (Fig. 5(a)). Its histogram appears slightly slenderer than a referential distribution associated with a commercial bulk gold standard (ΔV_{Au-Si}) and HOPG ($\Delta V_{HOPG-Si}$). Full Width at Half Maximum (FWHM) associated with these distributions is 0.0170 V for the gold standard, 0.0152 for the HOPG, and 0.0149 V for the QFS graphene. The shape of the histograms

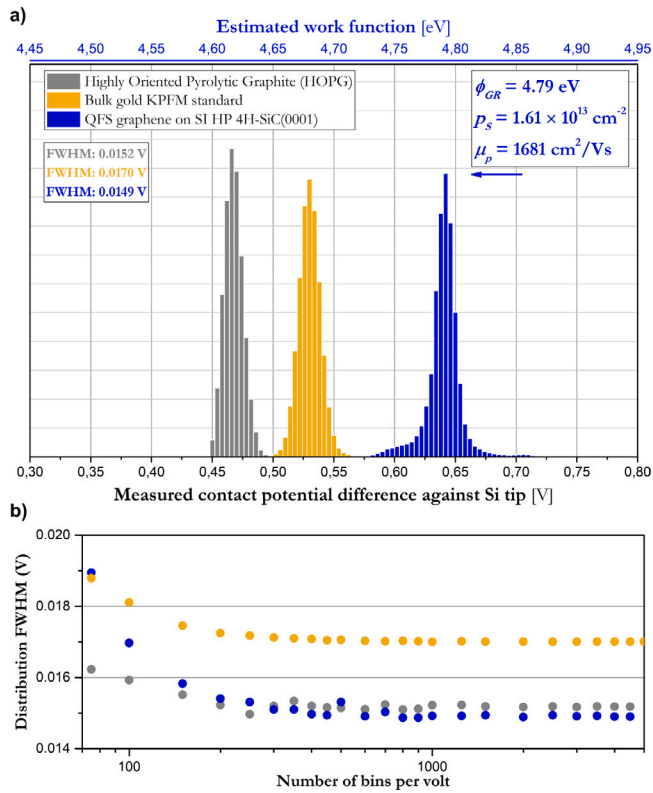


Fig. 5. (a) Distribution of the relative contact potential between the QFS graphene and the silicon tip, measured within the $10\text{-}\mu\text{m} \times 10\text{-}\mu\text{m}$ region of Kelvin Probe Force Microscopy analysis, marked in yellow in Fig. 1. For comparison, the figure is enriched with data associated with highly oriented pyrolytic graphite (HOPG) (gray) and a commercial bulk Au reference standard (golden). The blue top axis is the estimated work function based on our algorithm. (b) Corresponding Full Width at Half Maximum of the distributions as a function of the number of histogram bins per volt. Visible is the saturation at 1000 bins per volt.

depends on the density of bins (number of bins per volt); therefore, the FWHM of a Gaussian fit to the bin tops relies on the number of displayed bins. Yet, it quickly saturates. In this work, it was assessed at 1000 bins per volt (Fig. 5(b)).

Following the algorithm laid in the Introduction section and the DFT discussion, the apex of the QFS graphene distribution $\Delta V_{GR-Si} = 0.64\text{ V}$ is to be associated with a work function $\phi_{GR} = 4.79\text{ eV}$ ($N = 1.74$ and $p_S = 1.61 \times 10^{13}\text{ cm}^{-2}$). At this point, ΔV_{GR-Si} and ϕ_{GR} can be used to determine the work function of any other material under study through $\phi_m = \phi_{GR} + e(V_{m-Si} - V_{GR-Si})$.

3.5. Stability of the QFS graphene standard over time

Since HOPG and QFS graphene proved almost identical FWHM of their relative contact potential distributions and are closely related carbon materials, both underwent an aging experiment to assess their vulnerability to storage conditions and surface contamination [36]. Initially, the QFS-graphene/4H-SiC(0001) structure had hole density $p_S = 1.61 \times 10^{13}\text{ cm}^{-2}$ and hole mobility $\mu_p = 1681\text{ cm}^2/\text{Vs}$. Then, the element was stored in a nitrogen closet for 150 days and had the Hall effect and the relative contact potential difference measurements repeated.

The repeated verification shall be labeled *Day 1*. On *Day 1*, its hole concentration proved $p_S = 1.80 \times 10^{13}\text{ cm}^{-2}$ and $\mu_p = 1640\text{ cm}^2/\text{Vs}$. The experiment continued on *Day 4* and *Day 5*. On *Day 4*: $p_S = 1.81 \times 10^{13}\text{ cm}^{-2}$ and $\mu_p = 1627\text{ cm}^2/\text{Vs}$, and on *Day 5*: $p_S = 1.81 \times 10^{13}\text{ cm}^{-2}$ and $\mu_p = 1623\text{ cm}^2/\text{Vs}$.

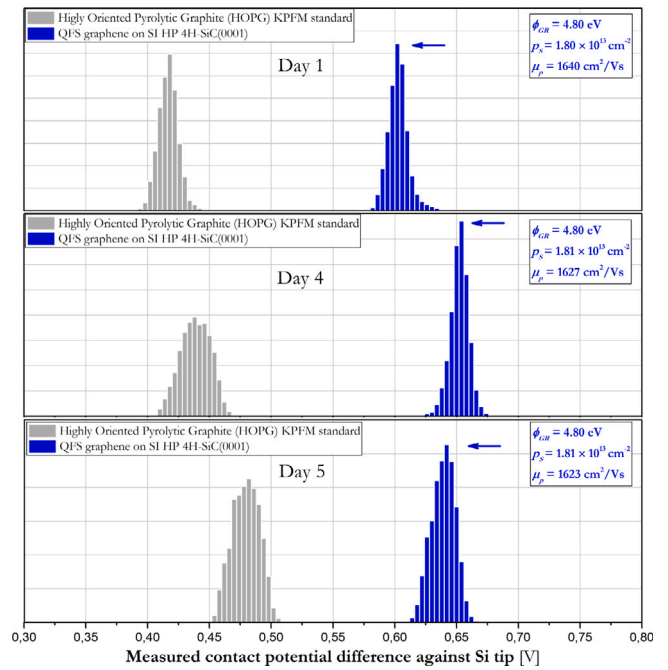


Fig. 6. Distribution of the relative contact potential between the QFS graphene and the silicon tip after 150 days in a nitrogen closet (*Day 1*), and then on *Day 4* and *Day 5*. The histograms are juxtaposed with referential HOPG (gray).

Fig. 6 illustrates the contact potential difference between the QFS graphene and the silicon tip on *Days 1–5*. The histograms are juxtaposed with referential HOPG. Since the number of the QFS graphene layers N did not change, only p_S was accounted for to read the DFT-calculated work function. Within the accuracy of our algorithm, it proved $\phi_{GR} = 4.80\text{ eV}$ on all *Days 1–5*, only 0.01 eV more than before the 150-day aging experiment.

Comparing Figs. 5 and 6, one can conclude that the contact potential difference associated with HOPG is not uniform over the 150-day aging experiment, both in the position and the distribution shape. Its apex falls in the range between $\Delta V_{HOPG-Si} = 0.42\text{ V}$ and $\Delta V_{HOPG-Si} = 0.48\text{ V}$. Accordingly, ΔV_{GR-Si} shifts between 0.60 V and 0.65 V and is not a monotonic function of the Hall-effect-derived hole density.

These suggest that the temporal stability of the silicon tip and environmental conditions may be pivotal to the KPFM analysis. Still, the expected location of the $\Delta V_{HOPG-Si}$ and ΔV_{GR-Si} within the differential voltage axis is limited to a relatively narrow sub- 0.1-eV range for both materials. Yet, unlike the HOPG sample, the QFS-graphene/4H-SiC(0001) structure is directly verifiable through spectroscopic ellipsometry (N) and the classical Hall effect (p_S) and may have its work function ϕ_{GR} updated based on N , p_S and our DFT-based algorithm.

4. Conclusions

We suggested a two-dimensional reference standard for the Kelvin Probe Force Microscopy method. The standard is a four-terminal mesa structure fabricated in the transfer-free p-type hydrogen-intercalated quasi-free-standing epitaxial Chemical Vapor Deposition graphene on semi-insulating high-purity nominally on-axis 4H-SiC(0001) technology.

The material of choice offers an atomic-flat surface within the (0001) terraces, elemental purity, and uniformity of charge carrier concentration. Once structured and wire-bonded, the QFS-graphene/4H-SiC(0001) is directly verifiable through a Hall effect measurement and guarantees efficient connection to the apparatus signal ground.

The particular structure had the hole density, $p_S = 1.61 \times 10^{13} \text{ cm}^{-2}$, determined via the classical direct current Hall effect. The statistical number of the QFS graphene layers, $N = 1.74$, was extracted from the analysis of the ellipsometric angle Ψ , measured at the angle of incidence $\text{AOI} = 50^\circ$ and the wavelength $\lambda = 490 \text{ nm}$. A Density Functional Theory model suggested that the work function of such QFS graphene is $\phi_{GR} = 4.79 \text{ eV}$.

The contact potential difference between the QFS graphene and the cantilever silicon tip proved to have a slender distribution around $\Delta V_{GR-Si} = 0.64 \text{ V}$. Its Full Width at Half Maximum was 0.0149 V , which was slightly lower than in a commercial bulk gold reference standard (0.0170 V) and on par with highly oriented pyrolytic graphite (0.0156 V).

We reason that $\Delta V_{GR-Si} = 0.64 \text{ V}$ can be associated with $\phi_{GR} = 4.79 \text{ eV}$ and applied as a precise reference value to calculate the work function of an arbitrary material under study. Thus, the QFS-graphene/4H-SiC(0001) system effectively complements bulk gold or cleaved highly oriented pyrolytic graphite as the reference standard.

Significantly, the Density Functional Theory model implies that even in a broad spectrum of the expected N and p_S for the QFS-graphene/4H-SiC(0001) technology ($N = 1.0$ to 2.0 , $p_S = 1.2$ to $2.0 \times 10^{13} \text{ cm}^{-2}$), the theorized work function is constrained to a relatively narrow $< 0.1\text{-eV}$ range between $\phi_{GR} = 4.77 \text{ eV}$ and $\phi_{GR} = 4.85 \text{ eV}$, adding to the precision of the standard.

A 150-day aging experiment proved that p_S rose from $1.61 \times 10^{13} \text{ cm}^{-2}$ to $p_S = 1.81 \times 10^{13} \text{ cm}^{-2}$, which, according to the Density Functional Theory model, up-shifted the work function by 0.01 V to $\phi_{GR} = 4.80 \text{ eV}$.

These changes are miniscule compared with the temporal stability of the Kelvin Probe Force Microscopy analysis, estimated at sub- 0.1 eV . This stability affects all reference standards, yet unlike gold or highly oriented pyrolytic graphite, the QFS-graphene/4H-SiC(0001) structure is directly and frequently verifiable. It may have its work function updated based on our algorithm.

CRedit authorship contribution statement

Tymoteusz Ciuk: Writing – original draft, Visualization, Validation, Supervision, Resources, Project administration, Methodology, Investigation, Funding acquisition, Formal analysis, Data curation, Conceptualization. **Beata Pyrzanowska:** Investigation, Data curation. **Jakub Jagiełło:** Software, Investigation, Formal analysis, Data curation. **Artur Dobrowolski:** Software, Investigation, Formal analysis, Data curation. **Dariusz Czołak:** Investigation. **Maciej J. Szary:** Writing – original draft, Software, Investigation, Formal analysis.

Declaration of competing interest

The authors declare that they have no known competing financial interests or personal relationships that could have appeared to influence the work reported in this paper.

Data availability

Data will be made available on request.

Acknowledgments

The research leading to these results has received funding from the National Science Centre, Poland, under Grant Agreement No. **OPUS 2019/33/B/ST3/02677** for the project “*Influence of the silicon carbide and the dielectric passivation defect structure on high-temperature electrical properties of epitaxial graphene*” and the National Centre for Research and Development, Poland, under Grant Agreement No. **M-ERA.NET3/2021/83/14BAGS/2022** for the project “*Ion Implantation for Innovative Interface Modifications in Battery and Graphene-enabled Systems*”. The M-ERA.NET3 has received funding from the European Union’s Horizon 2020 research and innovation programme under Grant Agreement No. **958174**.

References

- [1] E.G. Castanon, A. Fernández Scarioni, H.W. Schumacher, S. Spencer, R. Perry, J.A. Vicary, C.A. Clifford, H. Corte-León, Calibrated kelvin-probe force microscopy of 2D materials using pt-coated probes, *J. Phys. Commun.* 4 (9) (2020) 095025, <http://dx.doi.org/10.1088/2399-6528/abb984>.
- [2] S. Mammadov, J. Ristein, J. Krone, C. Raidel, M. Wanke, V. Wiesmann, F. Speck, T. Seyller, Work function of graphene multilayers on SiC(0001), *2D Mater.* 4 (1) (2017) 015043, <http://dx.doi.org/10.1088/2053-1583/4/1/015043>.
- [3] C. Melios, V. Panchal, C.E. Giusca, W. Strupinski, S.R.P. Silva, O. Kazakova, Carrier type inversion in quasi-free standing graphene: studies of local electronic and structural properties, *Sci. Rep.* 5 (1) (2015) 10505, <http://dx.doi.org/10.1038/srep10505>.
- [4] O. Kazakova, V. Panchal, T.L. Burnett, Epitaxial graphene and graphene-based devices studied by electrical scanning probe microscopy, *Crystals* 3 (1) (2013) 191–233, <http://dx.doi.org/10.3390/cryst3010191>.
- [5] W.N. Hansen, G.J. Hansen, Standard reference surfaces for work function measurements in air, *Surf. Sci.* 481 (1) (2001) 172–184, [http://dx.doi.org/10.1016/S0039-6028\(01\)01036-6](http://dx.doi.org/10.1016/S0039-6028(01)01036-6), URL <https://www.sciencedirect.com/science/article/pii/S0039602801010366>.
- [6] A. Kahn, Fermi level, work function and vacuum level, *Mater. Horiz.* 3 (2016) 7–10, <http://dx.doi.org/10.1039/C5MH00160A>.
- [7] S. Sinha, M. Mukherjee, A study of adventitious contamination layers on technically important substrates by photoemission and NEXAFS spectroscopies, *Vacuum* 148 (2018) 48–53, URL <https://api.semanticscholar.org/CorpusID:102569913>.
- [8] C.H. Kim, C.D. Bae, K.H. Ryu, B.K. Lee, H.J. Shin, Local work function measurements on various inorganic materials using kelvin probe force microscopy, in: *Advances in Nanomaterials and Processing*, in: *Solid State Phenomena*, vol. 124, Trans Tech Publications Ltd, 2007, pp. 607–610, <http://dx.doi.org/10.4028/www.scientific.net/SSP.124-126.607>.
- [9] N. Turetta, F. Sedona, A. Liscio, M. Sambì, P. Samorì, Au(111) surface contamination in ambient conditions: Unravelling the dynamics of the work function in air, *Adv. Mater. Interfaces* 8 (10) (2021) 2100068, <http://dx.doi.org/10.1002/admi.202100068>.
- [10] J. Lecoq, J. Bellier, C. Koehler, Comparison of crystallographic anisotropy effects on potential of zero charge and electronic work function for gold 111, 311, 110 and 210 orientations, *Electrochim. Acta* 35 (9) (1990) 1383–1392, [http://dx.doi.org/10.1016/0013-4686\(90\)85010-K](http://dx.doi.org/10.1016/0013-4686(90)85010-K), URL <https://www.sciencedirect.com/science/article/pii/001346869085010K>.
- [11] T.-H. Tran, R.D. Rodriguez, M. Salerno, A. Matković, C. Teichert, E. Sheremet, Twisted graphene in graphite: Impact on surface potential and chemical stability, *Carbon* 176 (2021) 431–439, <http://dx.doi.org/10.1016/j.carbon.2021.01.152>, URL <https://www.sciencedirect.com/science/article/pii/S0008622321001743>.
- [12] R. Bai, N.L. Tolman, Z. Peng, H. Liu, Influence of atmospheric contaminants on the work function of graphite, *Langmuir* 39 (34) (2023) 12159–12165, <http://dx.doi.org/10.1021/acs.langmuir.3c01459>.
- [13] C. Melios, A. Centeno, A. Zurutuza, V. Panchal, C.E. Giusca, S. Spencer, S.R.P. Silva, O. Kazakova, Effects of humidity on the electronic properties of graphene prepared by chemical vapour deposition, *Carbon* 103 (2016) 273–280, <http://dx.doi.org/10.1016/j.carbon.2016.03.018>, URL <https://www.sciencedirect.com/science/article/pii/S000862231630207X>.
- [14] T. Glatzel, M. Rusu, S. Sadewasser, M.C. Lux-Steiner, Surface photovoltage analysis of thin CdS layers on polycrystalline chalcopyrite absorber layers by kelvin probe force microscopy, *Nanotechnology* 19 (14) (2008) 145705, <http://dx.doi.org/10.1088/0957-4484/19/14/145705>.
- [15] P.A. Fernández Garrillo, B. Grévin, N. Chevalier, L. Borowik, Calibrated work function mapping by kelvin probe force microscopy, *Rev. Sci. Instrum.* 89 (4) (2018) URL <https://www.scopus.com/inward/record.uri?eid=2-s2.0-85045089599&doi=10.1063%2f1.5007619&partnerID=40&md5=d2431a5dc50c52fd8377165232a328f6>.
- [16] C. Sommerhalter, T.W. Matthes, T. Glatzel, A. Jäger-Waldau, M.C. Lux-Steiner, High-sensitivity quantitative Kelvin probe microscopy by noncontact ultra-high-vacuum atomic force microscopy, *Appl. Phys. Lett.* 75 (2) (1999) 286–288, <http://dx.doi.org/10.1063/1.124357>.
- [17] T. Ciuk, W. Strupinski, Statistics of epitaxial graphene for Hall effect sensors, *Carbon* 93 (2015) 1042–1049, <http://dx.doi.org/10.1016/j.carbon.2015.06.032>.
- [18] T. Ciuk, P. Caban, W. Strupinski, Charge carrier concentration and offset voltage in quasi-free-standing monolayer chemical vapor deposition graphene on SiC, *Carbon* 101 (2016) 431–438, <http://dx.doi.org/10.1016/j.carbon.2016.01.093>.
- [19] A. Dobrowolski, J. Jagiełło, T. Ciuk, K. Pięta, E.B. Możdżyńska, Layer-resolved Raman imaging and analysis of parasitic ad-layers in transferred graphene, *Appl. Surf. Sci.* 608 (2023) 155054, <http://dx.doi.org/10.1016/j.apsusc.2022.155054>.
- [20] J. Ristein, S. Mammadov, T. Seyller, Origin of Doping in Quasi-Free-Standing Graphene on Silicon Carbide, *Phys. Rev. Lett.* 108 (24) (2012).
- [21] J. Stawińska, H. Aramberri, M. Muñoz, J. Cerdá, Ab initio study of the relationship between spontaneous polarization and p-type doping in quasi-free-standing graphene on H-passivated SiC surfaces, *Carbon* 93 (2015) 88–104, <http://dx.doi.org/10.1016/j.carbon.2015.05.025>.

- [22] A. Dobrowolski, J. Jagiełło, K. Piętak-Jurczak, M. Wzorek, D. Czołak, T. Ciuk, Spectroscopic properties of close-to-perfect-monolayer quasi-free-standing epitaxial graphene on 6H SiC(0001), *Appl. Surf. Sci.* 642 (2024) 158617, <http://dx.doi.org/10.1016/j.apsusc.2023.158617>, URL <http://dx.doi.org/10.1016/j.apsusc.2023.158617>.
- [23] A. Dobrowolski, J. Jagiełło, D. Czołak, T. Ciuk, Determining the number of graphene layers based on Raman response of the SiC substrate, *Physica E 134* (May) (2021) 114853, <http://dx.doi.org/10.1016/j.physe.2021.114853>.
- [24] T. Ciuk, C. Nouvellon, F. Monteverde, B. Stańczyk, K. Przyborowska, D. Czołak, S. El-Ahmar, High-temperature thermal stability of a graphene hall effect sensor on defect-engineered 4H-SiC(0001), *IEEE Electron Device Lett.* (2024) <http://dx.doi.org/10.1109/led.2024.3436050>.
- [25] T. Ciuk, S. Cakmakyapan, E. Ozbay, P. Caban, K. Grodecki, A. Krajewska, I. Pasternak, J. Szmids, W. Strupinski, Step-edge-induced resistance anisotropy in quasi-free-standing bilayer chemical vapor deposition graphene on SiC, *J. Appl. Phys.* 116 (12) (2014) 123708, <http://dx.doi.org/10.1063/1.4896581>.
- [26] W. Strupinski, K. Grodecki, A. Wyszomolek, R. Stepniewski, T. Szkopek, P.E. Gaskell, A. Grüneis, D. Haberer, R. Bozek, J. Krupka, J.M. Baranowski, Graphene epitaxy by chemical vapor deposition on SiC, *Nano Lett.* 11 (4) (2011) 1786–1791, <http://dx.doi.org/10.1021/nl200390e>.
- [27] M.J. Szary, S. El-Ahmar, T. Ciuk, The impact of partial h intercalation on the quasi-free-standing properties of graphene on SiC(0001), *Appl. Surf. Sci.* 541 (2021) 148668, <http://dx.doi.org/10.1016/j.apsusc.2020.148668>.
- [28] T. Ciuk, O. Petruk, A. Kowalik, I. Jozwik, A. Rychter, J. Szmids, W. Strupinski, Low-noise epitaxial graphene on SiC Hall effect element for commercial applications, *Appl. Phys. Lett.* 108 (22) (2016) 223504, <http://dx.doi.org/10.1063/1.4953258>.
- [29] P. Giannozzi, S. Baroni, N. Bonini, M. Calandra, R. Car, C. Cavazzoni, D. Ceresoli, G.L. Chiarotti, M. Cococcioni, I. Dabo, A.D. Corso, S. de Gironcoli, S. Fabris, G. Fratesi, R. Gebauer, U. Gerstmann, C. Gougoussis, A. Kokalj, M. Lazzeri, L. Martin-Samos, N. Marzari, F. Mauri, R. Mazzarello, S. Paolini, A. Pasquarello, L. Paulatto, C. Sbraccia, S. Scandolo, G. Sclauzero, A.P. Seitsonen, A. Smogunov, P. Umari, R.M. Wentzcovitch, QUANTUM ESPRESSO: a modular and open-source software project for quantum simulations of materials, *J. Phys.: Condens. Matter.* 21 (39) (2009) 395502, <http://dx.doi.org/10.1088/0953-8984/21/39/395502>.
- [30] P. Giannozzi, O. Andreussi, T. Brumme, O. Bunau, M.B. Nardelli, M. Calandra, R. Car, C. Cavazzoni, D. Ceresoli, M. Cococcioni, N. Colonna, I. Carnimeo, A.D. Corso, S. de Gironcoli, P. Delugas, R.A.D. Jr, A. Ferretti, A. Floris, G. Fratesi, G. Fugallo, R. Gebauer, U. Gerstmann, F. Giustino, T. Gorni, J. Jia, M. Kawamura, H.-Y. Ko, A. Kokalj, E. Küçükbenli, M. Lazzeri, M. Marsili, N. Marzari, F. Mauri, N.L. Nguyen, H.-V. Nguyen, A.O. de-la Roza, L. Paulatto, S. Poncè, D. Rocca, R. Sabatini, B. Santra, M. Schlipf, A.P. Seitsonen, A. Smogunov, I. Timrov, T. Thonhauser, P. Umari, N. Vast, X. Wu, S. Baroni, Advanced capabilities for materials modelling with QUANTUM ESPRESSO, *J. Phys.: Condens. Matter.* 29 (46) (2017) 465901, URL <http://stacks.iop.org/0953-8984/29/i=46/a=465901>.
- [31] P. Giannozzi, O. Baseggio, P. Bonfà, D. Brunato, R. Car, I. Carnimeo, C. Cavazzoni, S. de Gironcoli, P. Delugas, F. Ferrari Ruffino, A. Ferretti, N. Marzari, I. Timrov, A. Urru, S. Baroni, QUANTUM ESPRESSO toward the exascale, *J. Chem. Phys.* 152 (15) (2020) 154105, <http://dx.doi.org/10.1063/5.0005082>.
- [32] H.J. Monkhorst, J.D. Pack, Special points for brillouin-zone integrations, *Phys. Rev. B* 13 (1976) 5188–5192, <http://dx.doi.org/10.1103/PhysRevB.13.5188>.
- [33] J. Heyd, G.E. Scuseria, M. Ernzerhof, Hybrid functionals based on a screened Coulomb potential, *J. Chem. Phys.* 118 (18) (2003) 8207–8215, <http://dx.doi.org/10.1063/1.1564060>.
- [34] S. Datta, P. Singh, D. Jana, C.B. Chaudhuri, M.K. Harbola, D.D. Johnson, A. Mookerjee, Exploring the role of electronic structure on photo-catalytic behavior of carbon-nitride polymorphs, *Carbon* 168 (2020) 125–134, <http://dx.doi.org/10.1016/j.carbon.2020.04.008>, URL <https://www.sciencedirect.com/science/article/pii/S0008622320303316>.
- [35] Łukasiewicz Research Network - Institute of Microelectronics and Photonics, Graphene epitaxy technologies, 2024, URL <http://www.graphene2get.com>.
- [36] T. Ciuk, Ł. Ciura, P. Michałowski, J. Jagiełło, A. Dobrowolski, K. Piętak, D. Kalita, M. Wzorek, R. Budzich, D. Czołak, A. Kolek, Contamination-induced inhomogeneity of noise sources distribution in Al₂O₃-passivated quasi-free-standing graphene on 4H-SiC(0001), *Physica E: Low-dimensional Systems and Nanostructures* 142 (2022) 115264, <http://dx.doi.org/10.1016/j.physe.2022.115264>.